Supplementary Information (SI) for Soft Matter.
This journal is © The Royal Society of Chemistry 2025

Investigation of microgel monolayers with the colloidal probe technique: How concentration and temperature allow tuning the properties of a microgel coating

T. Kratzenberg,[†] S. Schog,[†] S. Bochenek,[†] M. F. Schulte,[†] and W. Richtering[*,†,¶]

[†]*Institute of Physical Chemistry, RWTH Aachen University, Landoltweg 2, D-52056 Aachen, Germany, European Union.*

[‡]*Institute of Physical Chemistry, University of Münster, D-48149 Münster, Germany, European Union.*

[¶]*DWI-Leibniz Institute for Interactive Materials, Forckenbeckstr. 50, D-52056 Aachen, Germany, European Union.*

E-mail: wrichtering@pc.rwth-aachen.de

Supplementary Information

Materials

N-Isopropylacrylamide (NIPAM) (Acros Organics, Belgium), *N,N'*-Methylenebis(acrylamide) (BIS) (Alfa Aesar, USA), *N*-(3-Aminopropyl)methacrylamide hydrochloride (APMH) (Polysciences Inc., USA), 2,2′-azobis(2-methylpropionamidine)-dihydrochloride (V50) (Sigma-Aldrich, USA), and cetyltrimethylammonium bromide (CTAB) (Fluka Biochemica, Switzerland) were used as received. All interface experiments were performed with ultra-pure water (Astacus2, membraPure GmbH, Germany) with a resistivity of 60 µS cm^{-1}. All solutions were prepared with bi-distilled water.

Microgel synthesis

The microgel synthesis was performed as described elsewhere.[1] Briefly, the monomer NIPAM (5.4546 g), the cross-linker BIS (0.3398 g) and the comonomer APMH (0.1474 g) were dissolved in 330 mL of bi-distilled water. The solution was heated to 65 °C and purged with nitrogen under constant stirring. After 1 hour a degassed solution of the surfactant CTAB (0.0334 g) in 20 mL water was added to the monomer solution and allowed to equilibrate for 30 minutes before adding a degassed initiator solution containing 0.2253 g of V50 dissolved in 20 mL of water. The reaction was carried out for 4 hours at 65 °C under constant stirring and nitrogen flow. The purification was executed by ultracentrifugation and redispersion of the microgels in bi-distilled water.

Dynamic Light Scattering

Dynamic light scattering measurements were performed in a temperature range from T = (15.0 ± 0.1) °C to T = (50.0 ± 0.1) °C in 2 °C increments. A toluene-filled temperature bath was used to match the glass cuvette's refractive index. The diluted microgel suspension had a refractive index of $n(\lambda_0) = 1.33$. The laser vacuum wavelength was $\lambda_0 = 633$ nm. The scattering vector $q = 4\pi/\lambda_0 \sin(\theta/2)$ was changed by varying the scattering angle, θ, in 20° increments from 30 to 150°. The hydrodynamic radius, $\mathrm{R_h}$, is computed from the diffusion coefficient via the Stokes-Einstein equation.

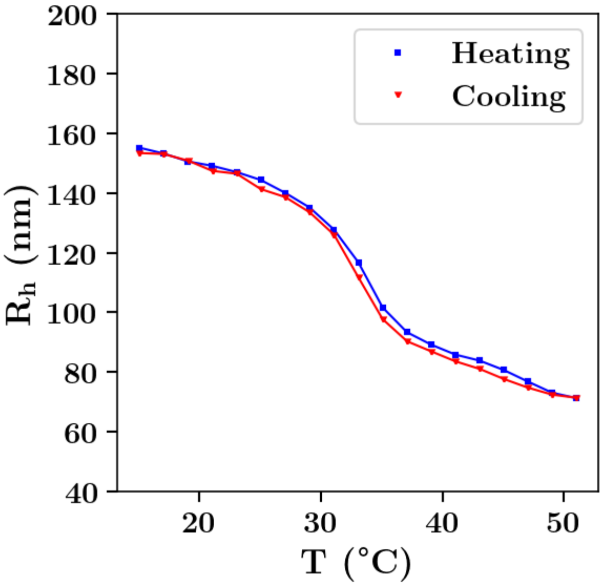

Fig. S1: Hydrodynamic radius R_h plotted against temperature for the investigated poly-*N*-Isopropylacrylamide microgels. The blue squares and red triangles show the heating and cooling cycle respectively.

Small-Angle Neutron Scattering

Small-angle neutron scattering experiments were performed at the KWS-2 instrument operated by Jülich Centre of Neutron Science at the Heinz Maier-Leibnitz Zentrum (Garchingen, Germany). The q-range was adjusted by varying the wavelength of the neutron beam between 0.5 and 1 nm and the sample-detector distance between 2, 8 and 20 m. The detector is a 2D-^{3}He tube-array consisting of 8 mm tubes and a $\Delta\lambda/\lambda$ of 10%.[2] Measurements were performed at 20 °C and 40 °C. Data were corrected accounting for sample transmission and dark count. The background of D_2O and D_2O/H_2O mixtures were subtracted from the data. The data were fitted using a fuzzy-sphere model. The respective data together with the model fits are shown in figure S2.

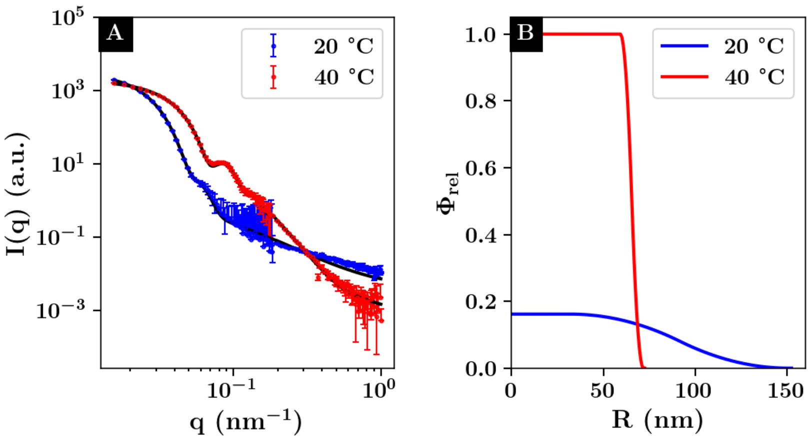

Fig. S2: (A) Scattering intensity $I(q)$ plotted against the wavevector q of PNIPAM microgels for measurements conducted at 20 and 40 °C. Black lines indicate the fit of the fuzzy-sphere model. (B) Relative polymer volume fraction Φ_{rel} plotted against the radius R from the microgel center from the fits of the fuzzy-sphere model at 20 and 40 °C respectively.

For comparison of the hydrodynamic Radius R_h with the radius of gyration R_g, the scattering data of the Guinier regime were additionally fitted (see figure S3).[3]

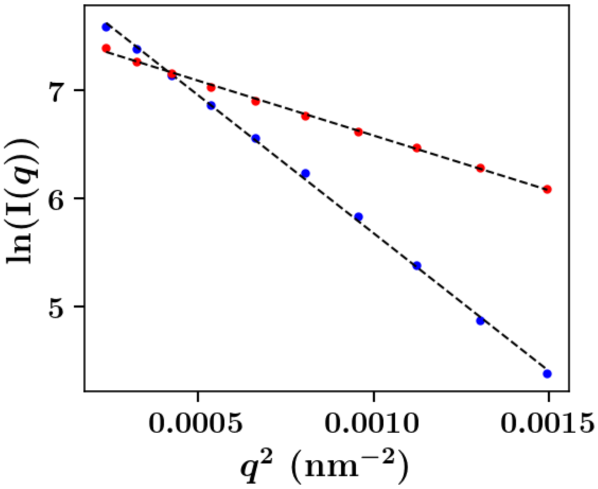

Fig. S3: Natural logarithm of the scattering intensity $I(q)$ plotted against the square of the wave vector $q < 0.04$ nm^{-1} below (blue dots) and above the volume phase transition temperature (VPTT) (red dots) together with linear regressions (dashed lines) for the determination of R_g.

The corresponding radii are summarized in table 1.

Table 1: Comparison of the hydrodynamic Radii R_h, the radius of gyration R_g and the ratio $R_\mathrm{g}/R_\mathrm{h}$ for the investigated microgel system below and above the volume phase transition temperature (VPTT).

T (°C)	R_h (nm)	R_g (nm)	$R_\mathrm{g}/R_\mathrm{h}$
20	(150 ± 3)	(88 ± 1)	(0.59 ± 0.02)
40	(88 ± 3)	(55 ± 1)	(0.62 ± 0.04)

The ratio of the radius of gyration R_g to the hydrodynamic radius R_h provides an important shape index which is linked to the volume phase transition temperature (VPTT) and the charge of the microgels.[4–6] As shown in table 1 the $R_\mathrm{g}/R_\mathrm{h}$ increases above the VPTT, which is in agreement with the literature.[4,7,8]

Deformation of Single microgels at the interface

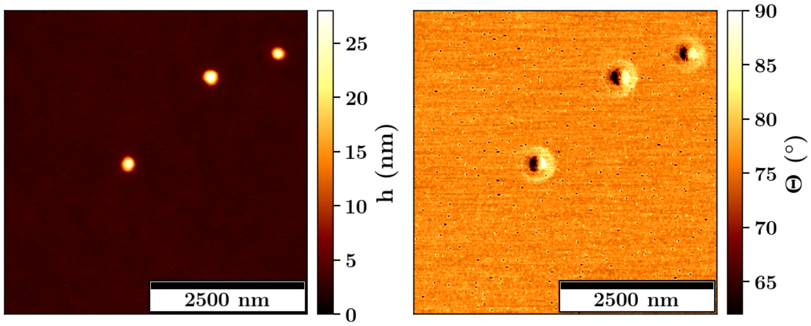

Fig. S4: Height (left) and phase image (right) of single microgels spin-coated on a Menzel glass with a 0.02 wt% microgel solution in 50 v% isopropanol.

Analysis of force volume measurements

The analysis of force-distance curves was carried out with a custom written *MATLAB* application (MathWorks, 2022b) based on the work of Schulte *et. al.*[9] Since the atomic force microscope (AFM) returns the cantilever deflection as a function of the relative scanner position, in the first step a baseline correction is performed, followed by a contact point determination based on a combination of a cumultative sum (cusum) algorithm and a minimum detection. The first calculates the magnitude of the standard deviation from the mean of the baseline data. The contact point is set where the moving mean of the data exceeds a multiple of this standard deviation. Here the multiplier is referred to as cusum threshold. To account for jump-to-contacts which can occur in the case of strong long-range attractive interactions, a second algorithm searches for minimum values in the approach curves. Here, the contact point is set to the minimum value if the minimum exceeds a threshold which is usually set to a value slightly above the noise level of the data. Figure S5 shows examples of the contact points determined in both cases. It should be noted that in the case of jump-to contacts, the actual contact point for soft matter is ill-defined, which is why setting the contact point to the minimum merely is in between the extreme cases of setting the contact point to the beginning or the end of the jump-to-contact at zero force.[10] The determination of the contact point allows the shift of the force-distance curve data to obtain force-indentation data which are used for further analysis e.g. to calculate stiffness. The baseline correction of the retraction curve is handled separately to account for the hydrodynamic drag out of contact with the sample. Because the baseline of the retraction curve is shorter compared to the approach curve, a subroutine controls the baseline fit to obtain similar gradient values compared to the approach curve. Thus, the adhesion force can be calculated from the minimum of the retraction curve. Further, the adhesion work is calculated from the trapezoidal numerical integration of the retraction data below the baseline. In a similar manner, the

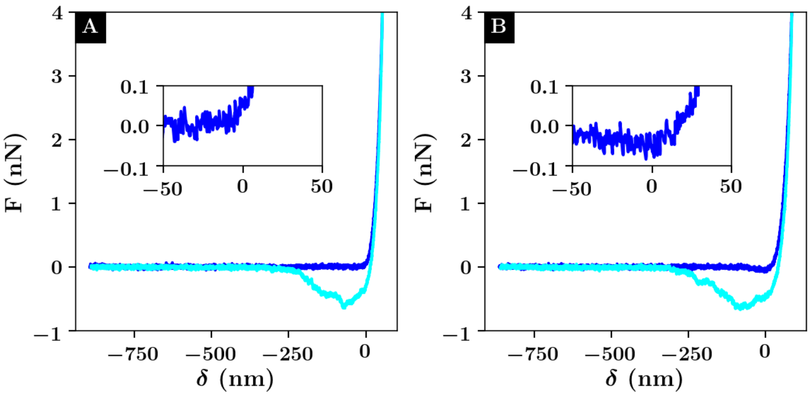

Fig. S5: (A) Example for a force curve where the contact point was determined with a cusum algorithm using a cusum threshold of 5. (B) Example of a force curve where the contact point was determined based on the minimum of the jump-to-contact.

dissipative energy is calculated from the integral of the approach and retraction data for which a positive force acts on the sample (equation 1).

$$W_{\mathrm{diss}} = \int_{\delta=0\,\mathrm{nm}}^{\delta_{\max}} F_{\mathrm{approach}}(\delta)\, d\delta - \int_{\delta(F_{\mathrm{retraction}}=0)}^{\delta_{\max}} F_{\mathrm{retraction}}(\delta)\, d\delta \tag{1}$$

The contact stiffness values are calculated from the local derivative of the force-indentation curve of the approach curve (equation 2).

$$k = \frac{dF_{\mathrm{approach}}}{d\delta} \tag{2}$$

To calculate the local derivative, the moving average of the data is interpolated with a piecewise cubic HERMITE interpolating polynomial using the *pchip* function in *Matlab*. A numerical gradient calculation of the interpolated data is then performed. Since the calculation of the stiffness data returns again a four-dimensional data set, cross-section of the data along the xy-direction can be obtained via linear interpolation along the stiffness data to generate stiffness profiles.

Fitting is performed by the *iMINUIT* package maintained by the Scikit-HEP project which is a python port of the *MINUIT2* library copyrighted by *CERN* maintained by the *CERN*'s *ROOT* team.

Generation of height and corrected height data

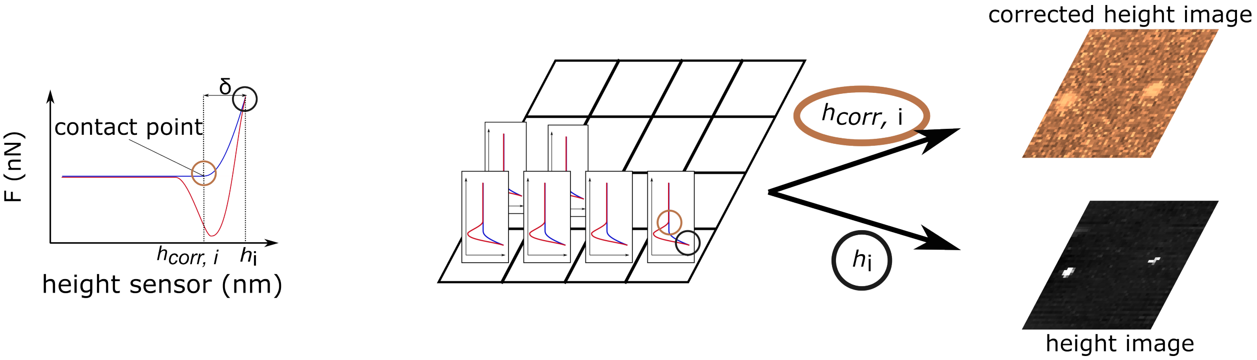

Fig. S6: Sketch of an idealized force-distance curve (left). The approach curve is shown in blue and the retraction curve is shown in red. The force curves show the different height data obtained for a force-distance curve. The height data directly obtained from the force volume measurement is the height h_i at the point on the force-distance curve at which the maximum force set for the measurement is exerted on the sample. The corrected height $h_\mathrm{corr,i}$ is the height at the determined contact point and is only obtained after the measurement.On the right, a sketch of the generation of the height and corrected height images from the force volume data is shown. The mesh represents the encoded x and y coordinates for each recorded force-distance curve representing a single pixel of a force volume measurement. By extracting the height h_i for each force-distance curve the height image is created (grey image on the right at the bottom). From the height h_i and the contact point determination the corrected height $h_\mathrm{corr,i}$ for each curve is obtained which can be mapped in a similar manner as the height image and yields the corrected height image (beige image on the right at the top).

Force spectroscopy on a single microgel

Directional effects in scanning of a single microgel

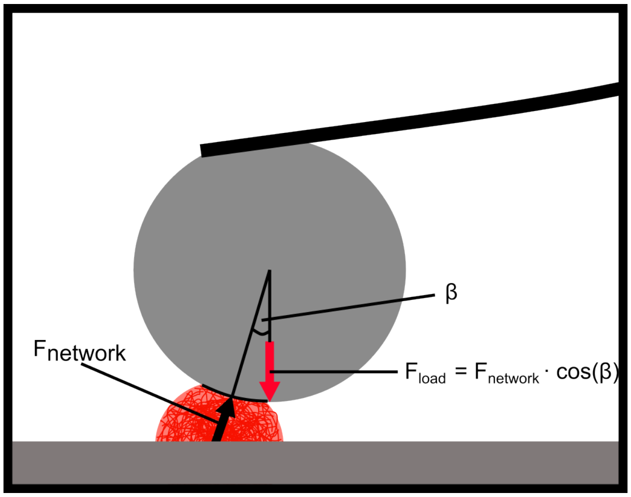

Fig. S7: Sketch for a non-symmetric case of indentation into a collapsed microgel. The sketch shows a colloidal probe in contact with the microgel together with relation between the applied normal load F_{load} and the counteracting force F_{network} from the microgel network.

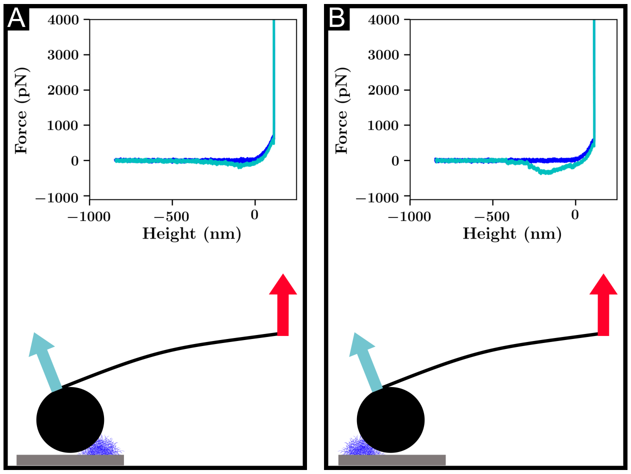

Fig. S8: Sketch of the force spectroscopy measurement performed on a single microgel. The sketch shows two force-distance curves (top) and a sketch with the position of the probe and the microgel (bottom) for different positions of the probe with respect to the microgel. The red arrow in the sketch indicates the movement of the scan head which is retracting from the sample. The blue arrow indicates the direction of the movement of the free cantilever end, which, due to the bending of the cantilever and the tilt towards the interface, is not perpendicular to the substrate.

Discussion of the choice of a fit function for the separation of force-distance curves

In figure S9, example force-distance curves for the measurement on a single microgel below the VPTT are shown.

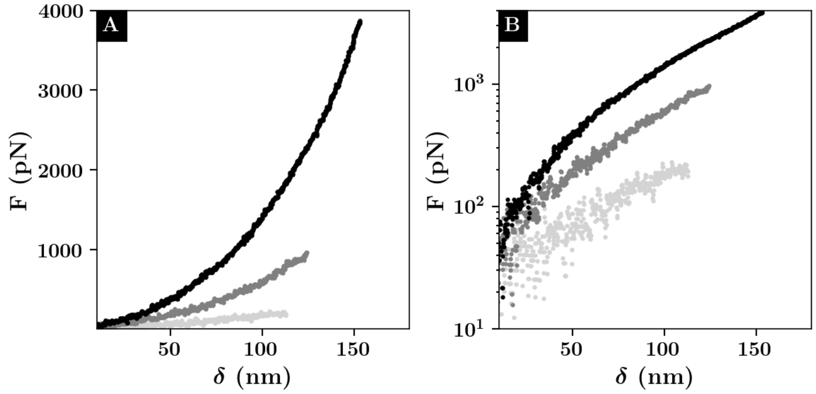

Fig. S9: Examples for force-distance curves recorded for the measurement of a single microgel below the VPTT in linear (A) and semi-log (B) representation. The curves are color-coded with respect to the distance from the microgel center. Black data points represent a curve recorded at the microgel center and light gray data points represent a curve recorded on the glass substrate.

The curves vary significantly with respect to their slope as well as the maximum deformation and force reached before the elasticity of the stiff substrate dominates the probe microgel interaction, i.e., the force drastically increases until the trigger threshold is reached. In order to describe the force-distance curves for the compression of a microgel, a Hertzian model has been used to describe the response of the network, e.g. by dividing the force curves into separate sections (see equation 3).[11–14]

$$F_{\text{Hertz}}(\delta, E^*) = \frac{4}{3} \cdot \sqrt{R} \cdot E^* \cdot \delta^{\frac{3}{2}} \tag{3}$$

Here, $F(\delta)$ describes the force measured with a spherical indenter with radius R as a function of the sample deformation δ for an homogeneous, infinite thick ideal elastic body.

However, this fails to describe the network response of a microgel over a larger deformation range due to the microgel's finite size and its heterogeneous polymer density distribution with respect to the lateral distance from the substrate (compare figure S10 A and B).[15]

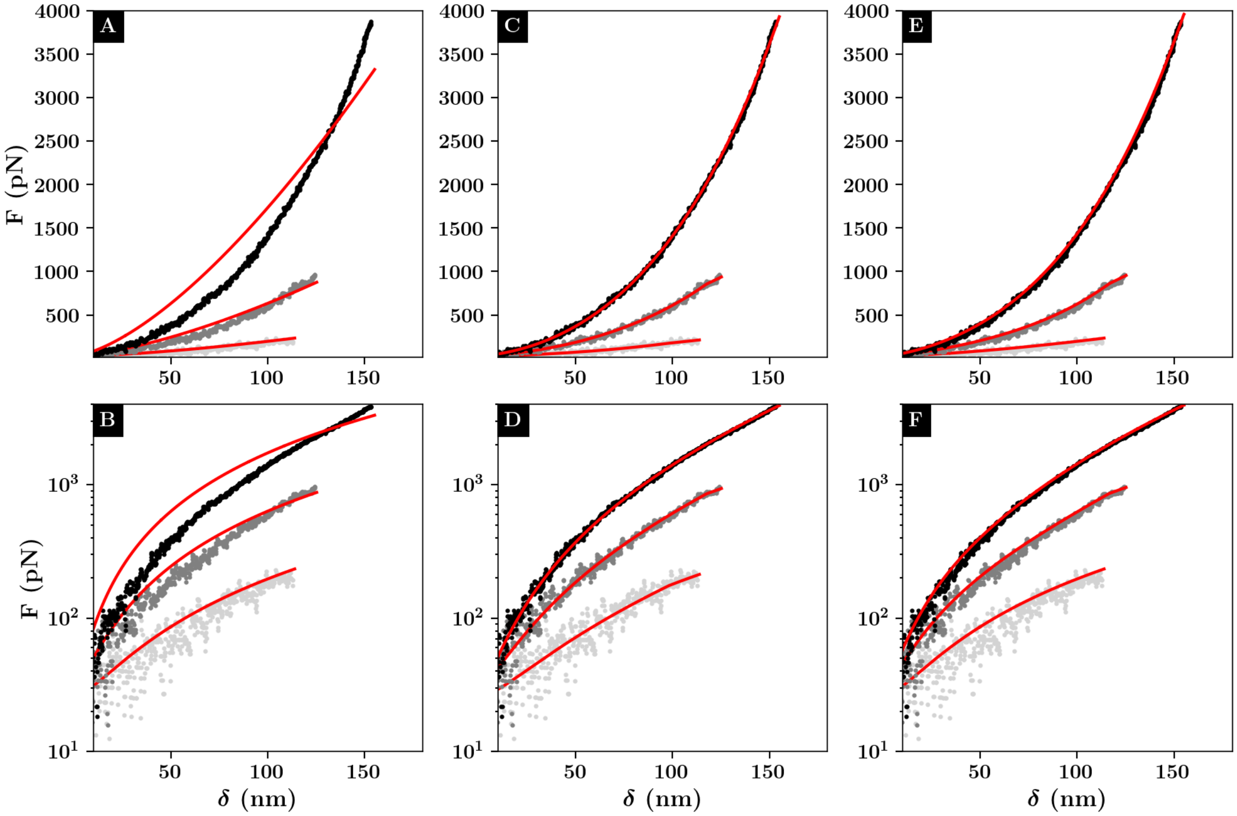

Fig. S10: Examples for force-distance curves recorded for the measurement of a single microgel below the VPTT in linear (top) and semi-log (bottom) representation with different model fits (red lines). The curves are color-coded with respect to the distance from the microgel center. Black data points represent a curve recorded at the microgel center and light gray data points represent a curve recorded on the glass substrate. (A, B) data fitted with a Hertzian model according to equation 3. (C, D) data fitted according to equation 8. (E,F) data fitted according to equation 8 with the profile function replaced according to equation 9.

The classical Hertz model can be corrected by assuming a smaller modulus for small amounts of deformation with respect to the modulus at high deformation.[12] Therefor, an arbitrary modifier function $p(\delta)$ can be used which accounts for a change in E^* dependent on δ (equation 4).

$$F(\delta) = p(\delta) \cdot F_{\text{Hertz}}(\delta, E^*) \tag{4}$$

We can choose the boundary conditions for $p(\delta)$ so that the change in E^* is described with respect to the E^* at maximum indentation by setting $p(\delta_{\max}) = 1$. The Hertz model for both the curves from the interactions of the colloid with the solid substrate and from the colloid with the microgel overestimates the measured load. In the case of the interactions with the solid substrate, for large separation distances the measured load can be approximated by equation 5 where σ_{probe} and σ_{surface} refer to the charge density of the probe and the substrate respectively and λ_{D} describes the Debye length.[16]

$$F_{\text{e}} = \frac{4\pi\sigma_{\text{probe}}\sigma_{\text{surface}}\lambda_{\text{D}}}{\epsilon_0\epsilon_{\text{m}}} \cdot e^{-\frac{d}{\lambda_{\text{D}}}} \tag{5}$$

The distance from the substrate d is related to the deformation by $d \approx \delta_{\max} - \delta$. Further, assuming similar interactions of the uncross-linked microgel corona with the probe compared to a polymer brush, the change in load can also be described by a simple exponential function.[17] We might thus also choose an exponential function as base for the description $p(\delta)$. Considering, that the initial scaling is smaller compared to E^*, a second boundary condition can be chosen so that $p(\delta = 0) = \epsilon, \epsilon \in (0, 1)$ where ϵ describes the change in the scaling factor at zero deformation for $F_{\text{Hertz}}(\delta = 0, E^* \cdot \epsilon)$ relative to $F_{\text{Hertz}}(\delta = \delta_{\max}, E^*)$. We can then allow for a change $p(\delta)$ modifying the exponential increase with a second parameter λ to allow for a change in the correction of the Hertz model depending on the type of force-curve used for the fitting. After normalization according to the first boundary condition, this yields equation 6 and 7.

$$p(\delta, \lambda, \epsilon) = \begin{cases} \frac{1-\epsilon}{e^1-1} \cdot e^{\left(\frac{\delta}{\lambda}\right)} + \frac{\epsilon \cdot e^1 - 1}{e^1 - 1} & \forall \quad 0 \le \delta \le \lambda, \forall \epsilon \in (0, 1) \\ 1 & \forall \quad \delta > \lambda \end{cases} \tag{6}$$

$$F(\delta) = \frac{4}{3} \cdot \sqrt{R} \cdot p(\delta, \lambda, \epsilon) \cdot E^* \cdot \delta^{\frac{3}{2}} \tag{7}$$

As the Hertz model assumes zero force for $\delta = 0$, and because the actual force curves have a minimum amount of noise of around 50 pN, for the fitting of the data, a fixed offset F_{offset}

based on the force at $\delta = 0$ is added to the fitting function (equation 8).

$$F(\delta) = \frac{4}{3} \cdot \sqrt{R} \cdot p(\delta, \lambda, \epsilon) \cdot E^{*} \cdot \delta^{\frac{3}{2}} + F_{\text{offset}} \tag{8}$$

As shown in figure S10 C and D, this yields reasonable fit results and allows for a clear distinction of the different force-distance curve types based on the fitted parameters E^{*}, ϵ and λ (compare figure S11 A).

We note that while the above-described approach yields reasonable fit results using a minimum number of variables, the choice of the profile function itself, although based on physical considerations, is arbitrary, and there exists a multitude of different options for the choice of a profile function $p(\delta)$. This is shown in figure S10 E and F, where the profile is replaced by the profile described in equation 9, which is derived following the same boundary conditions, and allowing for a variable base in addition to a variable exponent $s \in (0, \infty)$.

$$p(\delta, \lambda, \epsilon, s) \begin{cases} (1-\epsilon) \cdot \left(\frac{\delta}{\lambda}\right)^{s} + \epsilon & \forall \quad 0 \leq \delta \leq \lambda, \forall \epsilon \in (0,1) \\ 1 & \forall \quad \delta > \lambda \end{cases} \tag{9}$$

For comparison of both profile functions, the resulting profiles from the fits according to equation 6 and 9 are plotted in figure S11. Both profiles related to the compression of the microgel show similar behavior for both equations. However, in the case of the curve recorded on the glass substrate, the profile function according to equation 9 is constant, which is equivalent to the fit of the pure Hertzian model (equation 3). This shows that the higher complexity of equation 9 with an additional variable leads to a loss of information. Thus, equation 9 is less suitable to separate the force-distance curves from each other.

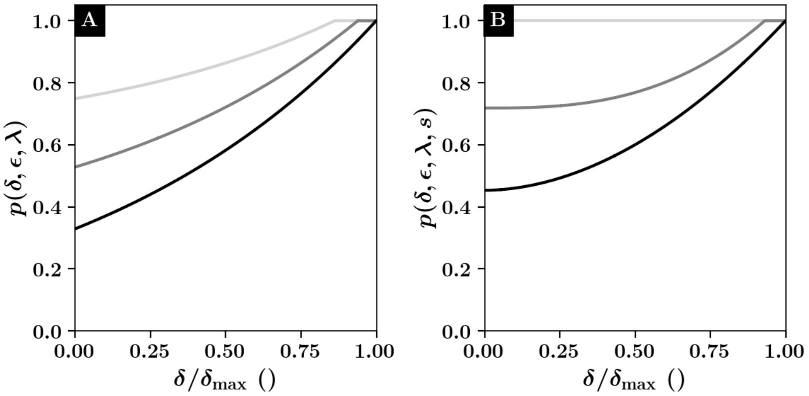

Fig. S11: Resulting profiles from the curves fitted in figure S10 using the same color coding plotted against the normalized deformation $\delta/\delta_{\mathrm{max}}$. (A) Fit results from the profile function according to equation 6. (B) Fit results from the profile function according to equation 9.

Evaluation of fit results

Figure S12 shows the product of ϵ and E^* representing the scaling factor at low indentation depth. Here, in contrast to the distribution of E^* a more homogeneous radial distribution is observed around the center of the microgel. A similar lateral distribution of high value of the product of $\epsilon \cdot E^*$ compared to the high values in the energy dissipation is observed (compare figure 4).

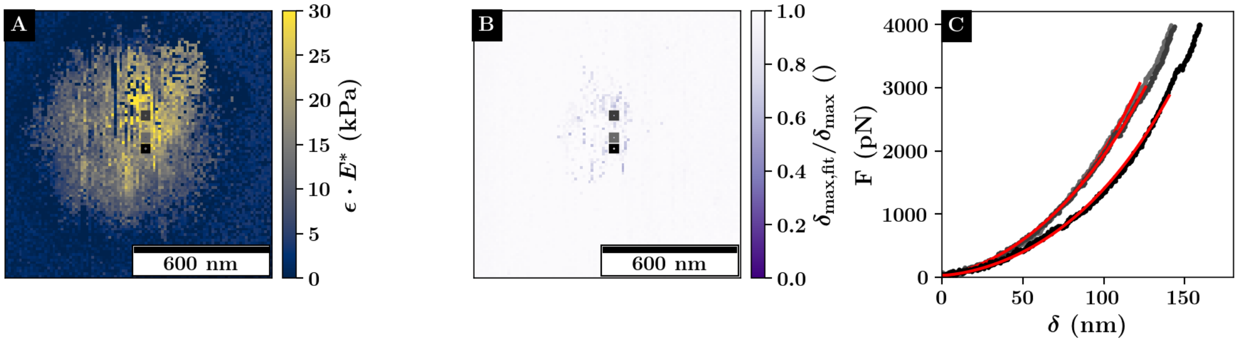

Fig. S12: Fit results for a single microgel at 27 °C below the VPTT. (A) Plot of the initial scaling at low indentation. (B) Relative amount of the data used for fitting the model function. (C) Example curves showing bad deviations from the model fit together with the respective fit.

Most of the measured force-distance curves contain a steep increase in the force at high indentation as a consequence of the stiff underlying substrate. Since the fit function does not account for the influence of the elasticity of the substrate on the measured repulsive interactions, the range of indentation for each individual curve was iteratively adjusted until the maximum of the residue was below 120 pN and 200 pN for the measurement at 27 °C and 40 °C respectively. The higher threshold at higher temperatures was necessary to achieve similar fits as the steeper increase in combination with deviations from the ideal elastic response resulted in a larger absolute error.

Figure S12 B represents the fitting range for which the model is valid. It shows the relative amount of the force-distance curve which is used for the data fit. In case of a good fit, the curve describes the force-distance curve over the full deformation range ($\delta_{\mathrm{max,fit}} = \delta_{\mathrm{max}}$) and the ratio of $\delta_{\mathrm{max,fit}}/\delta_{\mathrm{max}}$ is one. If parts of the force-distance curve deviate from the model, $\delta_{\mathrm{max,fit}} < \delta_{\mathrm{max}}$, and the ratio of $\delta_{\mathrm{max,fit}}/\delta_{\mathrm{max}}$ is smaller then one. The map shows predominantly white pixels and a smaller amount of darker pixels close to the center of the microgel.

This indicates that the fitting function describes the shape of the force-distance curve well for the majority of the data.

The darker values correspond to fits for which not the whole curve could be fitted. Examples are given in Figure S12 C. These curve have in common, that they show a rather abrupt change in the slope at high indentation. This can occur in the case of plastic deformation, network inhomogeneities or a force-induced slip of the probe.[18,19] Considering that their is no indication for a systematic change in the curves as the scan progresses, a plastic-deformation of the network is unlikely. Nevertheless, the model function describes the curve shape rather well below the VPTT.

Above the VPTT, the deviation between the data and the model fit, accumulate at the transition between the compression of the microgel and the interaction with the pure substrate (figure S12).

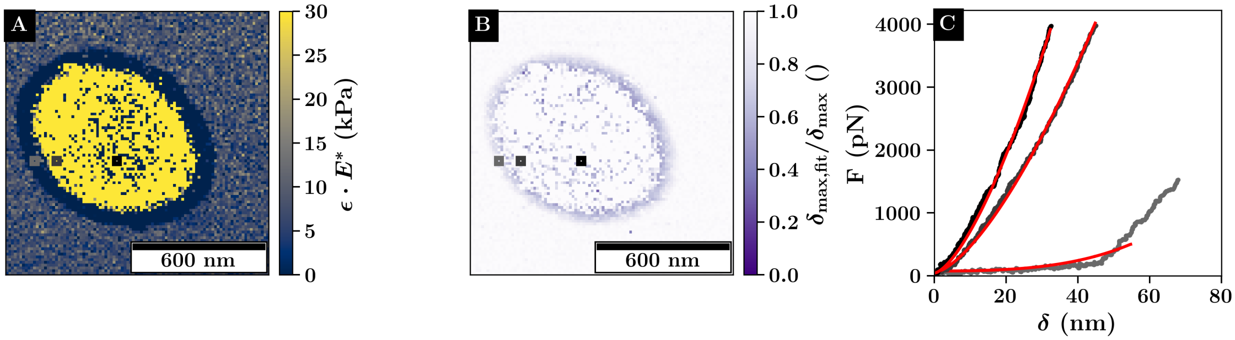

Fig. S13: Fit results for a single microgel at 40 °C above the VPTT. (A) Plot of the initial scaling at low indentation. (B) Relative amount of the data used for fitting the model function. (C) Example curves showing bad deviations from the model fit together with the respective fit.

At these positions the model fit fails. This is because the transition from the Coulomb interaction between the probe and the substrate and the interaction between the probe and the microgel network shows a rather abrupt change in the force-distance curve's slope (compare figure S13 C).

Nevertheless, the same transition in the data at these positions can be derived from the model fit, allowing for a separation of the force-distance curves.

Force spectroscopy on microgel monolayers

Example Force curves for M1 and M2

In figure S14 example for force-distance curves recorded for M1 and M2 are displayed. Notably, there exist a large difference in the retraction curves below and above the VPTT (cyan an orange curves)(compare figure S14 A and B and C and D). Below the VPTT the adhesion force, represented by the retraction curves minima, is increased for M2 in comparison to M1. Further, the width of adhesion represented by the width of the retraction curve smaller then the 0 nN is increased for M2. This can be attributed to the larger monolayer deformation as well as the interactions with more microgels in the case of M2.

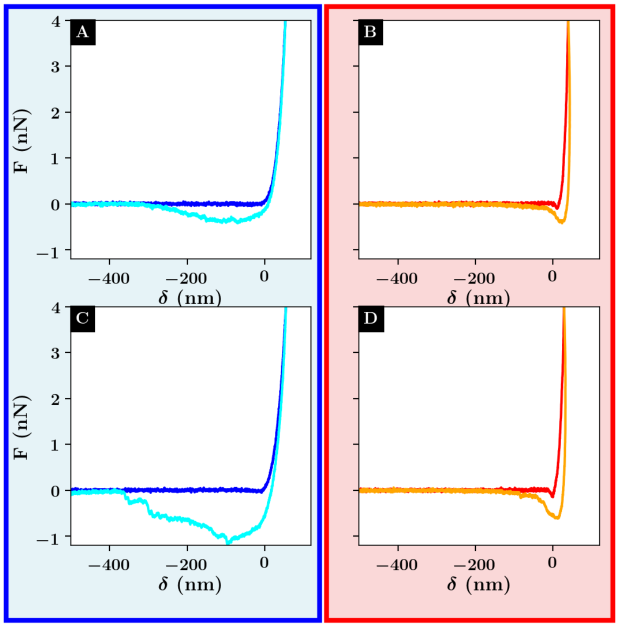

Fig. S14: Example force-indentation curves of monolayers M1 (A, B) and M2 (C, D) below (left) and above the VPTT (right). Approach curves are displayed in blue and red and retraction curves in cyan and orange respectively.

Above the VPTT, the adhesion force as well as the adhesion width are reduced. This indicates that less PNIPAM chains and or less microgels contribute to the total attractive probe monolayer interactions as compared to the swollen monolayers.

The curves above the VPTT further feature jump-to-contacts (JTCs) which are represented by a minimum of the approach curve at $\delta = 0$ nm.

Deformations of monolayers, M1, and M2

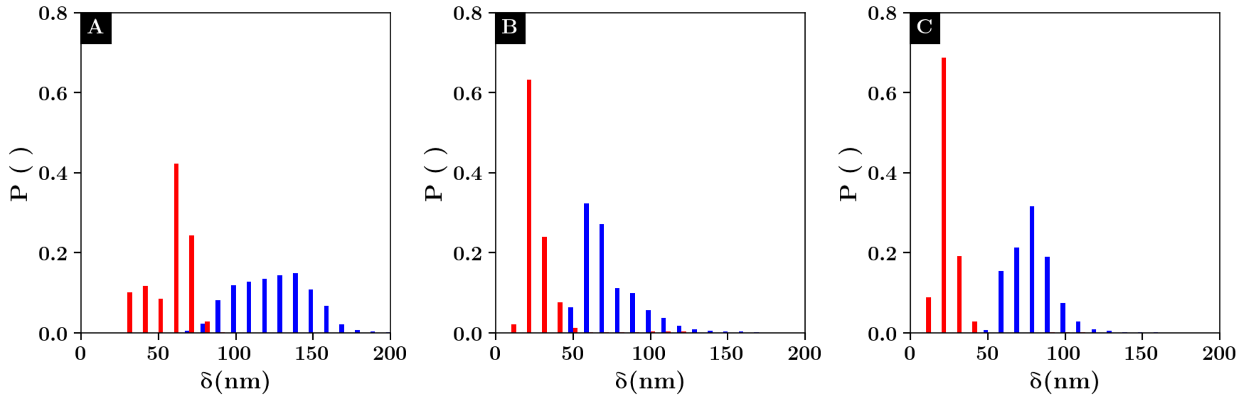

Fig. S15: Relative probability plotted against indentation depth for force volume measurements for the measurement of a single microgel (A) and microgel monolayers M1 (B) and M2 (C). Measurements at 27 °C below the VPTT correspond to the blue distributions. Measurements at 40 °C above the VPTT correspond to the red distributions. The sample size is a minimum of 6400.

Dissipative Energy histogramms for M1 and M2

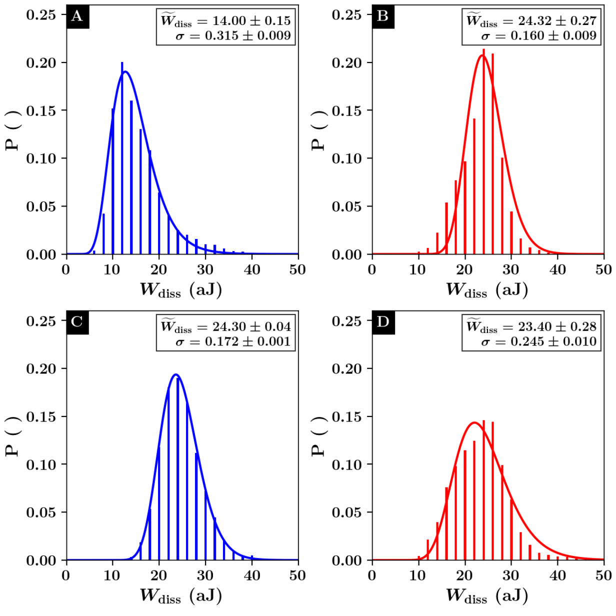

Fig. S16: Relative probability plotted against the energy dissipation for force volume measurements performed on monolayer M1 (A, B) and M2 (C, D) bellow the VPPT (left, blue) and above the VPTT (red, right). The distributions were fitted with a log-normal distribution (solid lines) returning the median of the dissipative energy distribution $\tilde{W}_{\text{diss}}$ and the standard deviation σ.

Film Homogeneity

Measurements on microgel monolayers were performed on at least two separate positions on the substrate to exclude differences in the probe-microgel interactions due to film defects. This is representatively shown for the image of adhesion force for monolayer M1 in figure S17.

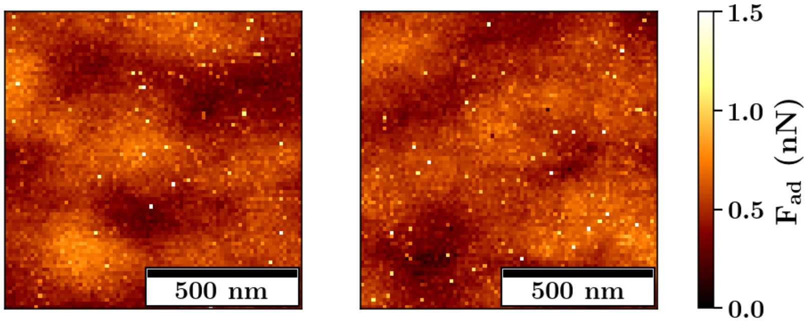

Fig. S17: Images of the adhesion force F_{ad} on monolayer M1 recorded at 27 °C recorded on two different positions on the substrate. Measurements were recorded with a scan size of 1 x 1 µm^2 and a resolution of 80 x 80 pixels.

Both images display similar magnitudes of adhesion force as well as spatial distributions of the measured adhesion. This suggests that the discussed measurements are representative for the monolayer.

Height and Corrected Height Images of M1 and M2

The corrected height images for monolayers M1 and M2 are shown in figure S18

The height images do not show directly the structure with respect to the underlying substrate. This is because of the probe size and the microgel concentration. As the probe interacts with the monolayer, microgels are being compressed at every position of the substrate. Thus, the relative height with respect to the substrate is not directly recorded and there exists an unknown height offset which is the minimum distance between the compressed microgels and the substrate. This is why the average height depicted in e.g. figure S18 A with approx 120 nm is smaller compared to the height of the individual microgel shown in figure 2.

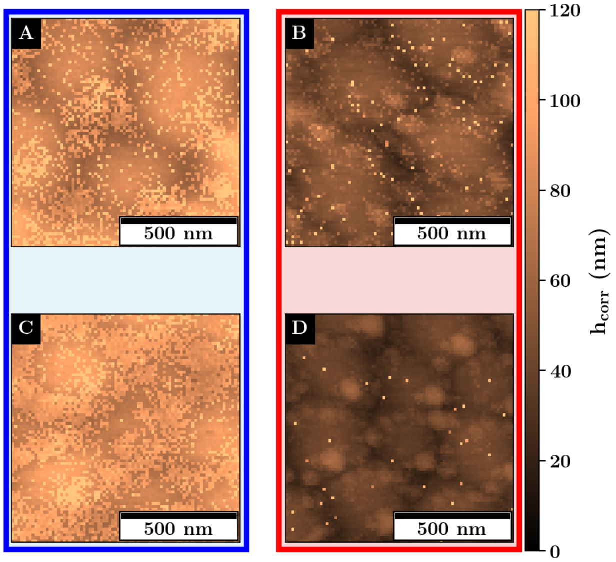

Fig. S18: Images of the corrected height h_{corr} on monolayers M1 (A, B) and M2 (C, D) recorded at 27 °C (left) and at 40 °C (right). Measurements were recorded with a scan size of 1 x 1 μm^2 and a resolution of 80 x 80 pixels.

The corrected height images below the VPTT in figure S18 A and C show larger round objects which depict the microgels in a hexagonal packing. In between the objects, the pixel with a larger height values are observed which match the pixels for which JTCs are measured.

The deviations from the structure as observed for lower height values of the monolayer are due to the inherent inaccuracy in the determination of the contact point in the case of the JTC for soft matter.[10]

It should be noted, that the inaccuracy in the contact point determination has a minor or no effect on the results discussed for the monolayers. As the results for e.g. the deformation are observed independent of the inclusion of the JTCs, as they span only a fraction of the total indentation into the sample.

Above the VPTT, the monolayers appear more heterogeneous. A hexagonal structure of the monolayer is indicated, similar to the swollen monolayers. However, there exist multiple local changes in height.

We attribute this to a rougher surface as the collapsed microgels are expected to have some polydispersity with respect to their height. This can be seen in the height image for the dry microgels (compare figure 6). The differences in height can result in a depiction of several microgels at once depending on the local roughness and the maximum deformation of the sample.

For completeness, the height images for the monolayers are depicted in figure S19.

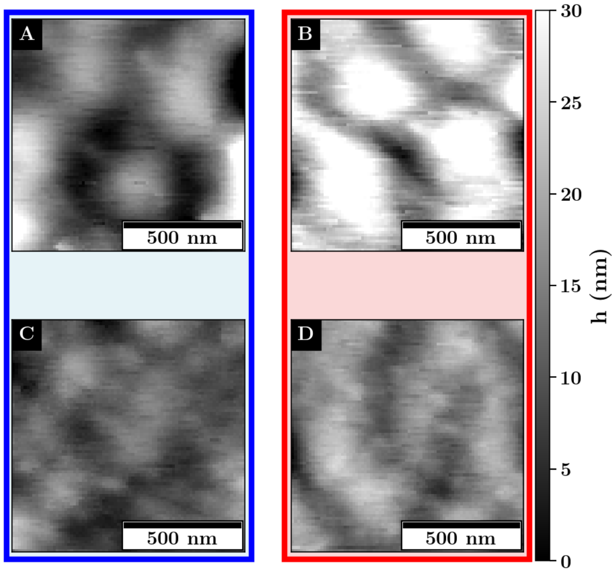

Fig. S19: Images of the height h on monolayers M1 (A, B) and M2 (C, D) recorded at 27 °C below the VPTT (left) and at 40 °C above the VPTT (right). Measurements were recorded with a scan size of 1 x 1 μm^2 and a resolution of 80 x 80 pixels.

The height images for M1 show more variance in the height compared to M2. As there are less microgels being compressed, the probe can better depict the valley in between the microgels.

To quantify the variance in the height and corrected height images the arithmetic roughness and the KURTOSIS roughness parameters were calculated.[20,21] Here, the arithmetic roughness R_a describes the average of the deviations from the mean surface height $\bar{h}$ (see equation 10).

$$R_\mathrm{a} = \frac{1}{N}\sum_{i=1}^{N} |h_\mathrm{i} - \bar{h}| \tag{10}$$

N is the number of height values and h_i is the height of the individual pixel.

The KURTOSIS roughness describes the sharpness of the height distribution, i.e., it is a measure of whether abrupt changes in the height values occur (equation 11).[20]

$$R_{\mathrm{ku}} = \frac{\frac{1}{N}\sum_{i=1}^{N}(h_{\mathrm{i}} - \bar{h})^4}{R_{\mathrm{rms}}^4} \tag{11}$$

R_{rms} describes the root mean square roughness which is the root of the squared deviation of the height and average height (equation 12).

$$R_{\mathrm{rms}} = \sqrt{\frac{1}{N}\sum_{\mathrm{i}=1}^{N}(h_{\mathrm{i}} - \bar{h})^2} \tag{12}$$

In figure S20 the arithmetic and KURTOSIS roughness are shown for the height and the corrected height images.

The arithmetic roughness of the of corrected height images in figure S20 shows a decrease in R_{a} from M1 and M2 both below and above the VPTT. The absolute values of R_{a} are smaller for the collapsed monolayer above the VPTT in comparison to the swollen monolayer below the VPTT.

The reduction in roughness from M1 to M2 are caused by the higher concentration of the microgels. This leads to less resolution of topographical height changes due to convolution. The change in the absolute value of R_{a} can be attributed to the reduction in average height for the monolayers above the VPTT. Thus, the arithmetic roughness is not suitable to describe the changes in roughness between the swollen and collapsed microgels, as the deswelling of the monolayer is accompanied by a large change in the average height.

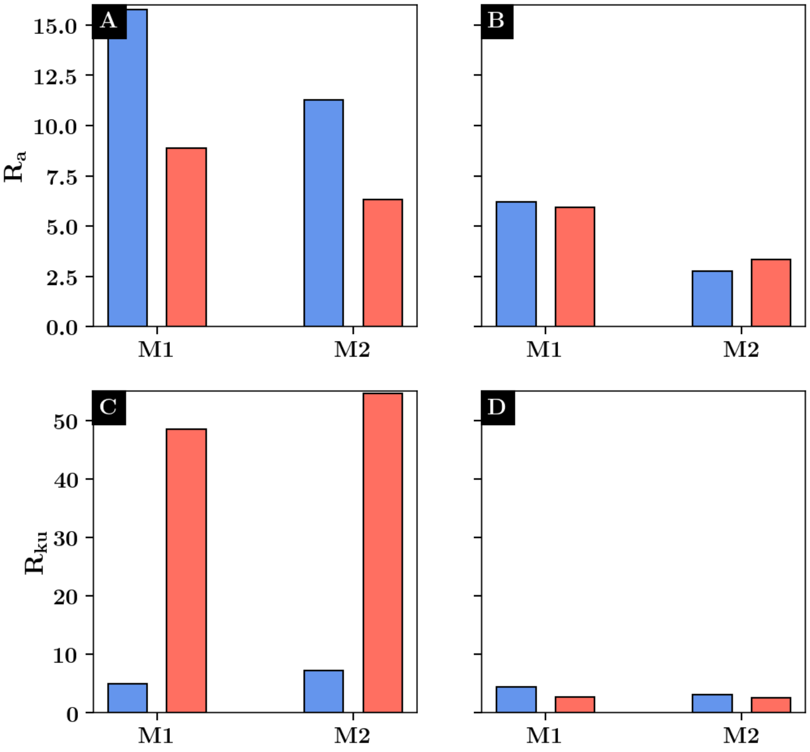

Fig. S20: Bar plot of the arithmetic roughness of the corrected height (A) and height data (B) for M1 and M2. Kurtosis roughness parameters for the corrected height (C) and height data (D) for M1 and M2. The blue bars represent the roughness parameters at 27 °C below the VPTT and the red bars represent the roughness parameters at 40 °C above the VPTT.

The Kurtosis roughness allows for a better comparison between different temperatures for the swollen and collapsed monolayers. This is shown for the corrected height data in figure S20 C. R_{ku} is drastically increased above the VPTT for M1 and M2 compared to R_{ku} below the VPTT. This quantitatively describes the sharper transition between the height data observed in the corrected height images above the VPTT.

The arithmetic roughness for the height image data shows similar trends as for the corrected height. This is in agreement with the observation made for the stiffness profiles, that profile of the height changes from M1 to M2. The Kurtosis roughness for the height images depicted in figure S20 for both monolayers is highly reduced in comparison to corrected height images.

Stiffness data

In figure S21 the calculated stiffness data are plotted against the normalized deformation for M1 and M2. The stiffness histograms describe the averaged response of the probed microgel film, rather than showing the local stiffness distribution shown in the stiffness profiles. Below the VPTT, the distribution of the stiffness values becomes narrower for M2 in figure S21 B in comparison to M1 in figure S21 A.

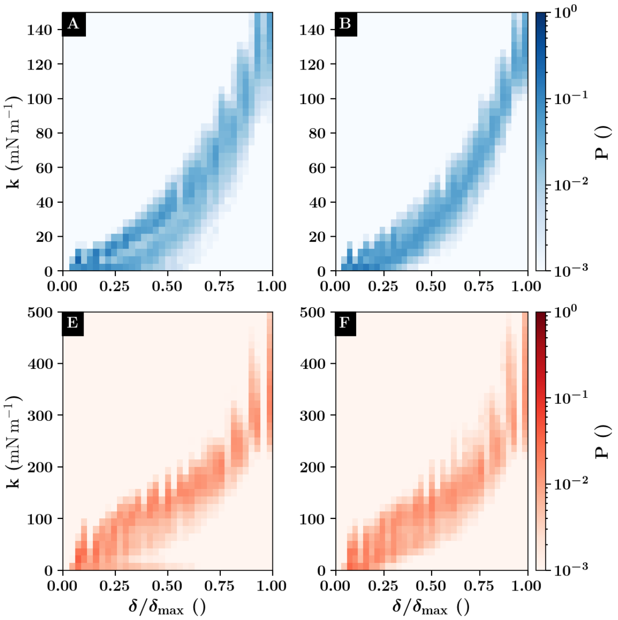

Fig. S21: Stiffness distribution plotted against the relative indentation depth recorded on M1 (left) and M2 (right) at 27 °C below the VPTT (top, blue) and 40 °C above the VPTT (bottom, red). The stiffness distribution is shown for 35 x 35 evenly spaced bins for the relative indentation depth and stiffness values ranging from either 1 to 150 $\mathrm{mN\,m^{-1}}$ (blue) or 1 to 500 $\mathrm{mN\,m^{-1}}$ (red). The force volume measurement was recorded on a 1 µm x 1 µm with a resolution of 80 x 80 px corresponding to 6400 force-distance curves.

Additionally, the distribution in figure S21 for M2 is shifted further to the right in comparison to M1. This represents the same stiffness is only reached at a higher percentage of the deformation.

The narrower distribution shows that, due to the higher microgel concentration, the elastic response becomes more homogeneous throughout the microgel monolayer.

Further, the shift in the stiffness distribution reflects the softening of the microgel monolayer as discussed for the stiffness profiles in figure 10.

Above the VPTT, the stiffness distributions show much higher stiffness values and a different shape of the distribution.

Further, a similar trend for the shift of the stiffness distribution can be observed between M1 and M2 with an increase in concentration. The occurrence of higher stiffness values is shifted towards higher values of the relative deformation.

However, both distribution display a more heterogeneous distribution in comparison to the histograms below the VPTT.

Similar to this, the distribution of the stiffness values with respect to the applied force is shown in figure S22.

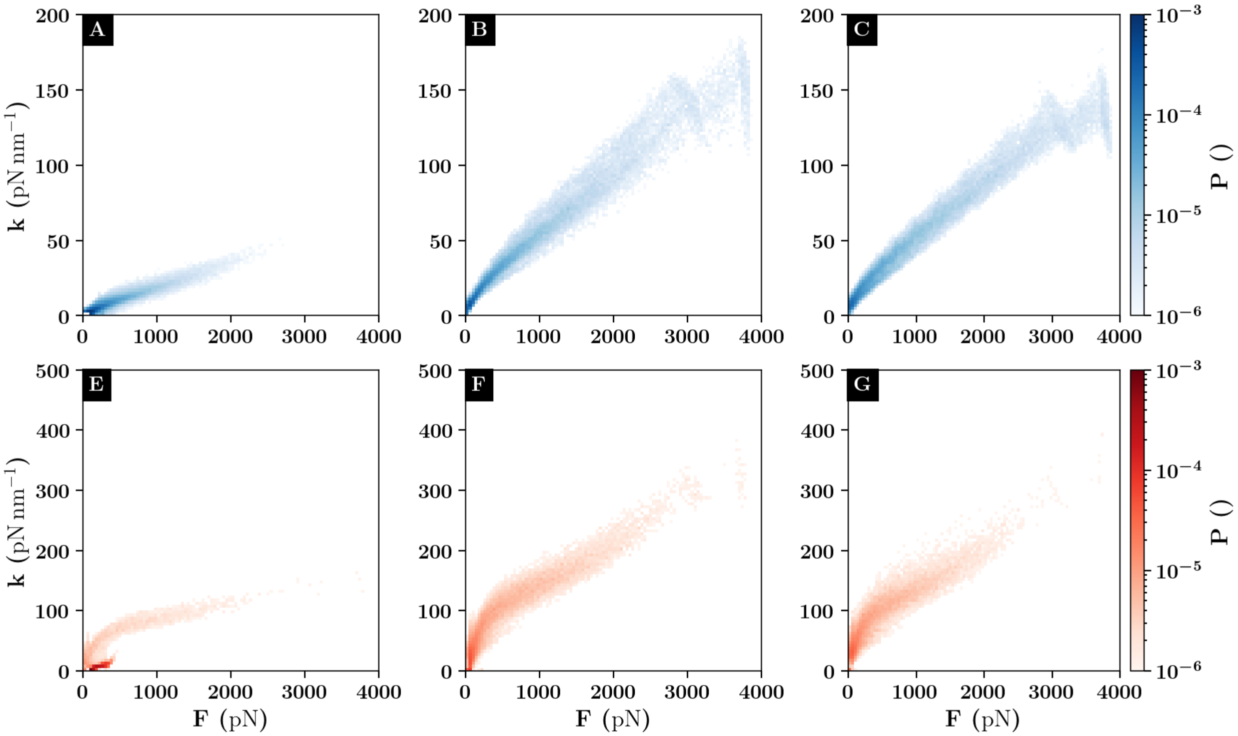

Fig. S22: Histogram of the stiffness data plotted against the applied load at 27 °C below the VPTT (top row, blue) and 40 °C above the VPTT (bottom row, red). The figure shows the distribution for the single microgel (A und E), at $N_{\mathrm{Area}} = (4.22\pm0.12)\ \mu\mathrm{m}^{-2}$ (B and F) and at $N_{\mathrm{Area}} = (6.10\pm0.15)\ \mu\mathrm{m}^{-2}$ for at least 6400 force-distance curves.

The distribution for the single microgel (figures S22 A and E) is much more shallow both bellow and above the VPTT because only the single microgel contributes to the net interactions.

Below the VPTT, a narrower distribution of the stiffness is observed for M2 compared to M1 (figure S22 B and C).

Above the VPTT, the stiffness values are more spread at a high load for M1 and M2 compared to the distributions below the VPTT (compare figures S22 F and G).

We attribute this to a variation in height for the individual microgels in combination with the large increase in the stiffness values. This results in larger variation in stiffness as more than one microgel is getting compressed while the monolayer is probed.

Microgel desorption and probe contamination

In figure S23 the image of the energy dissipation for an example measurement on a monolayer in the third compression regime is shown (compare figure 6 M3).

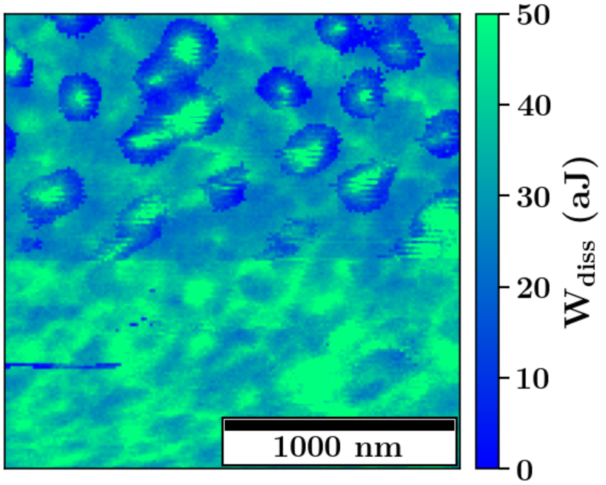

Fig. S23: Dissipative energy image of a microgel monolayer with $N_{\text{area}} = (8.04 \pm 0.65)\ \mu\text{m}^{-2}$ in the third compression regime for M3. The Force volume measurement was performed at 27 °C below the VPTT with 2 µm x 2 µm scan size and a resolution of 160 x 160 pixels. The scan was performed from bottom to top.

The scan direction is from bottom to top and alternating left to right or right to left. The image shows an abrupt change in the magnitude of the energy dissipation alongside with the appearance of local minima in the energy dissipation which show a similar two dimensional structure compared to the dry monolayer. The change in the magnitude of the energy dissipation suggest a change of the probe interface. This would influence convolution due to a change of the probes surface topography and a change in the probe microgel interactions.

References

(1) Bochenek, S.; Scotti, A.; Ogieglo, W.; Fernández-Rodríguez, M. Á.; Schulte, M. F.; Gumerov, R. A.; Bushuev, N. V.; Potemkin, I. I.; Wessling, M.; Isa, L.; Richtering, W. Effect of the 3D Swelling of Microgels on Their 2D Phase Behavior at the Liquid-Liquid Interface. *Langmuir : the ACS journal of surfaces and colloids* **2019**, *35*, 16780–16792.

(2) Houston, J. E.; Brandl, G.; Drochner, M.; Kemmerling, G.; Engels, R.; Papagiannopoulos, A.; Sarter, M.; Stadler, A.; Radulescu, A. The high-intensity option of the SANS diffractometer KWS-2 at JCNS - characterization and performance of the new multi-megahertz detection system. *Journal of Applied Crystallography* **2018**, *51*, 323–336.

(3) Guinier, A.; Fournet, G.; Walker, C. B.; Yudowitch, K. L. *Small-angle Scattering of X-rays / André Guinier ; Gérard Fournet. Transl. [aus d. Ms.] by Christopher B[land] Walker. Followed by a bibliography by Kenneth L. Yudowitch*; Structure of Matter Series; Wiley [u.a.]: New York, 1955.

(4) Del Monte, G.; Truzzolillo, D.; Camerin, F.; Ninarello, A.; Chauveau, E.; Tavagnacco, L.; Gnan, N.; Rovigatti, L.; Sennato, S.; Zaccarelli, E. Two-step deswelling in the Volume Phase Transition of thermoresponsive microgels. *Proceedings of the National Academy of Sciences* **2021**, *118*.

(5) Kok, C. M.; Rudin, A. Relationship between the hydrodynamic radius and the radius of gyration of a polymer in solution. *Die Makromolekulare Chemie, Rapid Communications* **1981**, *2*, 655–659.

(6) Haydukivska, K.; Blavatska, V.; Paturej, J. Universal size ratios of Gaussian polymers with complex architecture: radius of gyration vs hydrodynamic radius. *Scientific Reports* **2020**, *10*, 14127.

(7) Roovers, J.; Martin, J. E. The hard–sphere model for linear and regular star polybutadienes. *Journal of Polymer Science Part B: Polymer Physics* **1989**, *27*, 2513–2524.

(8) Elancheliyan, R.; Chauveau, E.; Truzzolillo, D. Impact of polyelectrolyte adsorption on the rheology of concentrated poly(N-isopropylacrylamide) microgel suspensions. *Soft Matter* **2023**, *19*, 4794–4807.

(9) Schulte, M. F.; Bochenek, S.; Brugnoni, M.; Scotti, A.; Mourran, A.; Richtering, W. Stiffness Tomography of Ultra-Soft Nanogels by Atomic Force Microscopy. *Angewandte Chemie International Edition* **2021**, *60*, 2280–2287.

(10) Butt, H.-J.; Cappella, B.; Kappl, M. Force measurements with the atomic force microscope: Technique, interpretation and applications. *Surface Science Reports* **2005**, *59*, 1–152.

(11) Backes, S.; von Klitzing, R. Nanomechanics and Nanorheology of Microgels at Interfaces. *Polymers* **2018**, *10*, 1–23.

(12) Aufderhorst-Roberts, A.; Baker, D.; Foster, R. J.; Cayre, O.; Mattsson, J.; Connell, S. D. Nanoscale mechanics of microgel particles. *Nanoscale* **2018**, *10*, 16050–16061.

(13) Burmistrova, A.; Richter, M.; Uzum, C.; Klitzing, R. v. Effect of cross-linker density of P(NIPAM-co-AAc) microgels at solid surfaces on the swelling/shrinking behaviour and the Young's modulus. *Colloid and Polymer Science* **2011**, *289*, 613–624.

(14) Burmistrova, A.; Richter, M.; Eisele, M.; Üzüm, C.; von Klitzing, R. The Effect of Co-Monomer Content on the Swelling/Shrinking and Mechanical Behaviour of Individually Adsorbed PNIPAM Microgel Particles. *Polymers* **2011**, *3*, 1575–1590.

(15) Schulte, M. F.; Izak-Nau, E.; Braun, S.; Pich, A.; Richtering, W.; Göstl, R. Microgels react to force: mechanical properties, syntheses, and force-activated functions. *Chemical Society Reviews* **2022**, *51*, 2939–2956.

(16) Butt, H.-J. Measuring electrostatic, van der Waals, and hydration forces in electrolyte solutions with an atomic force microscope. *Biophysical Journal* **1991**, *60*, 1438–1444.

(17) Hans-Jürgen ButtMichael Kappl, Henning Mueller, Roberto Raiteri, Wolfgang Meyer, Jürgen Rühe Steric Forces Measured with the Atomic Force Microscope at Various Temperatures. *Langmuir* **1999**, 2559–2565.

(18) Kaliappan, S. K.; Cappella, B. Temperature dependent elastic–plastic behaviour of polystyrene studied using AFM force–distance curves. *Polymer* **2005**, *46*, 11416–11423.

(19) Dimitriadis, E. K.; Horkay, F.; Maresca, J.; Kachar, B.; Chadwick, R. S. Determination of Elastic Moduli of Thin Layers of Soft Material Using the Atomic Force Microscope. *Biophysical Journal* **2002**, *82*, 2798–2810.

(20) Gadelmawla, E. S.; Koura, M. M.; Maksoud, T.; Elewa, I. M.; Soliman, H. H. Roughness parameters. *Journal of Materials Processing Technology* **2002**, *123*, 133–145.

(21) Sedlaček, M.; Podgornik, B.; Vižintin, J. Correlation between standard roughness parameters skewness and kurtosis and tribological behaviour of contact surfaces. *Tribology International* **2012**, *48*, 102–112.